EUV spectroscopy of Sn^{5+}–Sn^{10+} ions in an electron beam ion trap and laser-produced plasmas

To cite this article: Z Bouza *et al* 2020 *J. Phys. B: At. Mol. Opt. Phys.* **53** 195001

View the article online for updates and enhancements.

EUV spectroscopy of Sn^{5+}–Sn^{10+} ions in an electron beam ion trap and laser-produced plasmas

Z Bouza[1,7] , J Scheers[1,2,7] , A Ryabtsev[3], R Schupp[1] , L Behnke[1],
C Shah[4,8] , J Sheil[1] , M Bayraktar[5] , J R Crespo López-Urrutia[4] ,
W Ubachs[1,2] , R Hoekstra[1,6] and O O Versolato[1,2]

[1] Advanced Research Center for Nanolithography, Science Park 106, 1098 XG Amsterdam, The Netherlands
[2] Department of Physics and Astronomy, and LaserLaB, Vrije Universiteit, De Boelelaan 1081, 1081 HV Amsterdam, The Netherlands
[3] Institute of Spectroscopy, Russian Academy of Sciences, Troitsk, Moscow 108840, Russia
[4] Max-Planck-Institut für Kernphysik, Saupfercheckweg 1, 69117 Heidelberg, Germany
[5] Industrial Focus Group XUV Optics, MESA+ Institute for Nanotechnology, University of Twente, Drienerlolaan 5, 7522 NB Enschede, The Netherlands
[6] Zernike Institute for Advanced Materials, University of Groningen, Nijenborgh 4, 9747 AG Groningen, The Netherlands

E-mail: o.versolato@arcnl.nl

CrossMark

Abstract
Emission spectra from multiply-charged Sn^{5+}–Sn^{10+} ions are recorded from an electron beam ion trap (EBIT) and from laser-produced plasma (LPP) in the extreme ultraviolet range relevant for nanolithographic applications. Features in the wavelength regime between 12.6 and 20.8 nm are studied. Using the Cowan code, emission line features of the charge-state-resolved Sn ion spectra obtained from the EBIT are identified. Emission features from tin LPP either from a liquid micro-droplet or planar solid target are subsequently identified and assigned to specific charge states using the EBIT data. For the planar solid tin target, the $4d$–$5p$ transitions of Sn^{8+}–Sn^{10+} ions are shown to dominate the long-wavelength part of the measured spectrum and transitions of type $4d$–$4f + 4p$–$4d$ are visible in absorption. For the droplet target case, a clear increase in the charge state distribution with increasing laser intensity is observed. This qualitatively demonstrates the potential of using long-wavelength out-of-band emission features to probe the charge states contributing to the strong unresolved transition array at 13.5 nm relevant for nanolithography.

Keywords: EUV spectroscopy, laser-produced plasma, electron beam ion trap, nanolithography

(Some figures may appear in colour only in the online journal)

1. Introduction

Highly charged Sn ions in laser-driven transient and dense plasmas are the emitters of extreme ultraviolet (EUV) light near 13.5 nm that is used in nanolithographic applications [1–4]. In such applications, hot plasma is produced when molten Sn microdroplets are illuminated by energetic laser

pulses. The responsible ions for emitting EUV photons near 13.5 nm are Sn^{8+}–Sn^{14+} with their resonance transitions $4p^6 4d^m$–$4p^5 4d^{m+1}$ and $4d^m$–$4d^{m-1} 4f$ ($m = 6$–0) [3–5]. Spectroscopic investigation of these plasmas is challenging due to the many, densely-packed transitions in these open-$4d$-subshell Sn ions. Furthermore, spectral lines belonging to adjacent ionic charge states may blend in wavelength. Charge-state-resolved measurements would facilitate line identifications in these complex systems. Such measurements can, e.g., be obtained from single-charge-state beam experiments of which the charge-exchange spectroscopy (CXS) of tin ions by Ohashi *et al* [6] is a notable example. Charge-state-resolved tin spectra can also be obtained from an electron beam ion trap (EBIT), using, e.g., matrix inversion techniques to deconvolve the mixed-charge-state EBIT spectra [7].

In EUV nanolithography machines, molybdenum-silicon multi-layer mirrors are used as projection optics. These optics are characterized by a 2% reflectivity bandwidth centered at 13.5 nm wavelength [8, 9]. The EUV radiation generated from the Sn laser-produced plasma (LPP) overlaps with the peak reflectivity of these mirrors. Most of the detailed spectroscopic studies in the literature focus on emission near 13.5 nm [3, 7, 10–18]. However the majority of the EUV emission occurs out-of-band, i.e., outside of the 2% reflectivity bandwidth [4]. From the application perspective, this out-of-band radiation reduces the efficiency of converting drive laser light into useful EUV photons. Moreover, such radiation can influence the optics lifetime or introduce unwanted thermal loads in the scanner [19, 20]. It is thus of particular interest and importance to quantify tin spectra over the full spectral band. Recent studies have shed light on the short-wavelength side of the out-of-band emission from LPP in the 7–12 nm range [21], complementing earlier work [13]. These insights regarding short-wavelength EUV radiation were subsequently used to obtain the relative contributions of charge states Sn^{9+}–Sn^{15+} to the main unresolved emission feature at 13.5 nm, and to successfully diagnose the plasma [22], obtaining, for instance, the temperature of an industrial EUV light source.

In this work, emission features of the multiply-charged Sn^{5+}–Sn^{10+} ions in the long-wavelength, 12.6–20.8 nm region are studied. Spectra are obtained from an EBIT and from LPP. Understanding the emission features enables quantifying the contributions in LPP from the lower charge states that could not be assessed from the previous short-wavelength studies [21, 22]. First, following the procedure outlined in reference [7], mixed-charge-state EBIT spectra are deconvolved to obtain single-charge-state spectra. Next, the line features from Sn^{5+}–Sn^{10+} ions are assigned using the semi-empirical Cowan code [23, 24], which allows for adjusting scaling factors in the calculation in order to fit observed spectra using initial preliminary assignments. These identifications are compared to literature where available. Finally, spectral features in the emission from Sn LPP, generated from liquid droplets as well as from planar solid tin targets over a wide range of laser intensities (and thus, plasma temperatures), are identified using the EBIT spectra. These investigations extend the set of diagnostic tools for monitoring EUV-producing tin LPP in an industrial setting.

2. Experiment

Two types of experiments are introduced in the following. First, the experimental setup used to record emission spectra of trapped Sn ions at the FLASH-EBIT facility [25] at the Max Planck Institute for Nuclear Physics in Heidelberg, Germany, is discussed. Second, experiments on laser-produced tin plasma that are carried out at the Advanced Research Center for Nanolithography (ARCNL) in Amsterdam, The Netherlands, are presented.

2.1. Electron beam ion trap (EBIT)

Spectroscopic measurements of Sn ions in the EUV regime have been performed using the FLASH-EBIT facility [25]. In an EBIT, an electron beam is used to trap, ionize, and excite ions for spectroscopic measurements. It enables the investigation of a wide range of Sn ion charge states. The FLASH-EBIT can deliver an electron beam with well-defined kinetic energies. A 6 T magnetic field is applied to guide and compress the electron beam down to a diameter of about 50 μm at the center of the trap. This magnetic field is generated by a pair of superconducting Helmholtz-coils. A molecular beam of tera-i-propyltin ($C_{12}H_{18}Sn$) is injected into the trap center region. Molecules are dissociated while crossing the electron beam. The electron beam rapidly excites, ionizes, and traps the Sn ions up to the desired charge state, while the lighter elements overcome the trapping potential and leave the EBIT. Trapping of a specific charge state can be achieved by adjusting the acceleration potentials that define the kinetic energy of the electron beam.

Radiation by the Sn ions is dispersed by a 1200 lines/mm flat-field, grazing-incidence grating with a variable line spacing [26] and is recorded on a Peltier-cooled charge-coupled device (CCD) camera. Background frames are recorded for the same exposure time as in the measurements with Sn present in the trap, and these images were then subtracted from the recorded plasma emission to eliminate the dark counts as well as read-out counts. The resulting CCD images are cropped and corrected for spectrometer aberrations. Subsequently, the images are integrated along the non-dispersive axis. The resulting spectra are then corrected for diffraction efficiency, as well as the quantum efficiency of the camera following reference [27] (also see, e.g., reference [28]). The wavelength calibration of the spectrometer is performed by injecting oxygen into the trap, using well-known O^{2+}–O^{4+} lines in the EUV range [29]. A wavelength range spanning 12.6–20.8 nm is captured with a resolution of about 0.03 nm at full-width-at-half-maximum (FWHM). A more detailed description of the EBIT experiments is given in references [7, 30, 31].

Two measurement series are conducted. In the first series, the electron-beam energy is increased from 60 to 200 eV in steps of 10 eV. The electron beam current is set to a constant 1.5 mA. Sn charge states 4^+ to 10^+ are observed using these EBIT settings. A two-dimensional map (wavelength–electron beam energy), composed by interpolating between discrete EBIT spectra, is presented in figure 1. In the second series, the electron beam energy is increased from 180 to 610 eV in
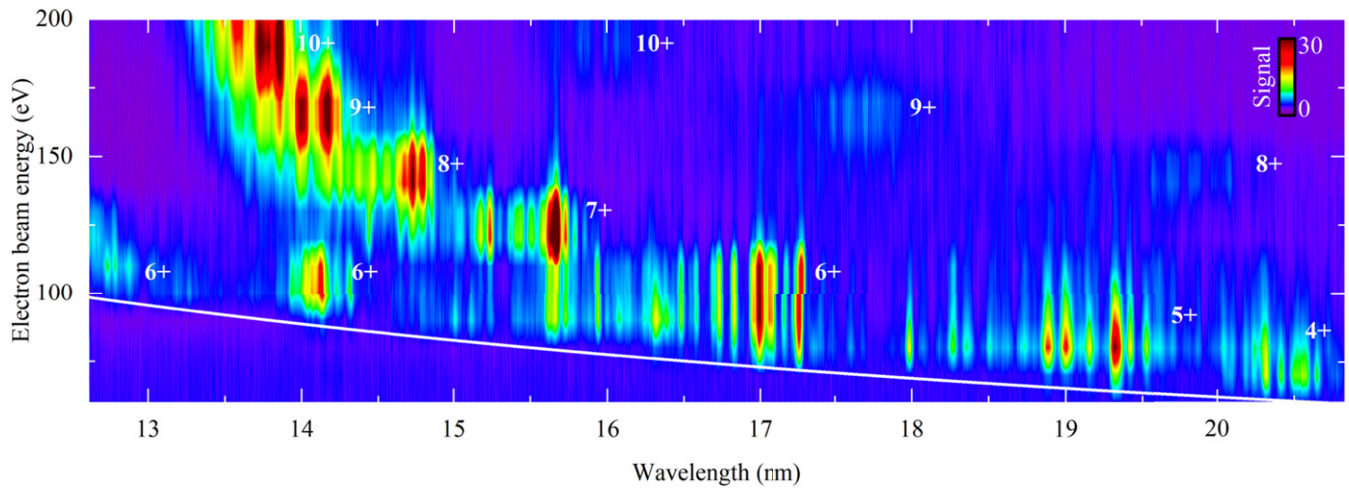
Figure 1. Two-dimensional spectral intensity map of Sn^{4+}–Sn^{10+} emission constructed from EBIT measurements (1.5 mA series). The map is produced by interpolating along the electron beam energy between discrete spectra which are taken at 10 eV steps. The colour bar indicates the signal or the emission intensity. The white line indicates where the electron beam energy equals the photon energy (see main text). Charge-state-specific emission islands are labeled by the charge state of the emitting Sn ion.

steps of 5 eV, and the electron beam current is set to a constant 13 mA. The Sn charge states that can be observed in this series range from 8^+ to 20^+.

2.2. Laser-produced plasma (LPP)

Two different experimental setups are used to produce Sn plasmas with a laser: (i) a droplet tin target and (ii) a planar solid tin target. Both experimental setups are detailed below. The targets are irradiated by a Nd:YAG laser operating at a wavelength of 1064 nm, with a Gaussian pulse length of 10 ns FWHM.

In both setups, spectral emission from the Sn-produced plasma is measured under an angle of $60°$ with respect to the propagation direction of the laser light, using a broadband transmission grating spectrometer [32, 33]. The spectrometer is operated with an entrance slit width of 25 μm and a 10 000 lines/mm transmission grating achieving an FWHM instrument resolution of 0.1 nm at 13 nm [32, 34]. The recorded wavelength regime is 5–25 nm. The diffracted light is recorded on a back-illuminated CCD from Greateyes (GE2048 512BI UV1), cooled to $-30°$C to reduce thermal noise. Background frames are recorded for the same exposure time as in the measurements with Sn plasma present, and these images were then subtracted from the recorded plasma emission to eliminate the dark counts as well as read-out noise. The exposure time is varied from 1–5 s to collect sufficient signal-to-noise ratio. The resulting CCD images are cropped and corrected for shear and tilt introduced by a slight misalignment of the slit and grating with respect to the CCD pixel array. Subsequently, the images are integrated along the non-dispersive axis. The resulting spectra are then corrected for first- and second-order diffraction efficiency, as well as the quantum efficiency of the camera.

The dispersion of the grating is obtained by observing well-documented Al^{3+} and Al^{4+} lines [29] from a laser-produced Al plasma [34]. Based on the position of the zeroth diffraction order, and known tin lines, an accurate wavelength calibration is obtained.

2.2.1. Droplet tin target. Molten Sn microdroplets of 99.995% purity with a diameter of 18 μm are dispensed from a droplet generator inside a vacuum vessel of 5×10^{-7} mbar pressure. The droplets travel at a speed of approximately 10 m s^{-1} in the vacuum vessel and pass through a horizontal light sheet produced by a He–Ne laser. The light scattered by the droplets is detected using a photomultiplier tube which subsequently triggers the Nd:YAG laser system. The droplets are irradiated by a laser pulse with an 80 μm (FWHM) Gaussian spot size. Additional details regarding the droplet-based experimental setup can be found in reference [35].

2.2.2. Planar solid tin target. A 1 mm thick Sn planar solid polycrystalline target of 99.995% purity is mounted onto a 2D-translation stage in a vacuum vessel which is kept at a pressure of 10^{-6} mbar. The solid target is irradiated by the same Nd:YAG laser system as is used for the droplet targets. The FWHM spot size at the planar target surface is 130 μm. Only two consecutive pulses are recorded on the same spot of the Sn target to prevent any influence of target deformation on the recorded spectra. The translation stage enables a step-wise motion of the target to guarantee a fresh target spot after each series of two pulses. Additional details regarding the planar solid-based experimental setup can be found in reference [36].

3. Measurements

In the following, we first discuss the results of the EBIT measurements. Spectra from individual charge states are presented (see figure 2), as obtained from EBIT measurements by using the matrix inversion introduced in reference [7]. Identifications of the observed line features are made using the Cowan code (figures 2 and 3). An overview of the wavelength
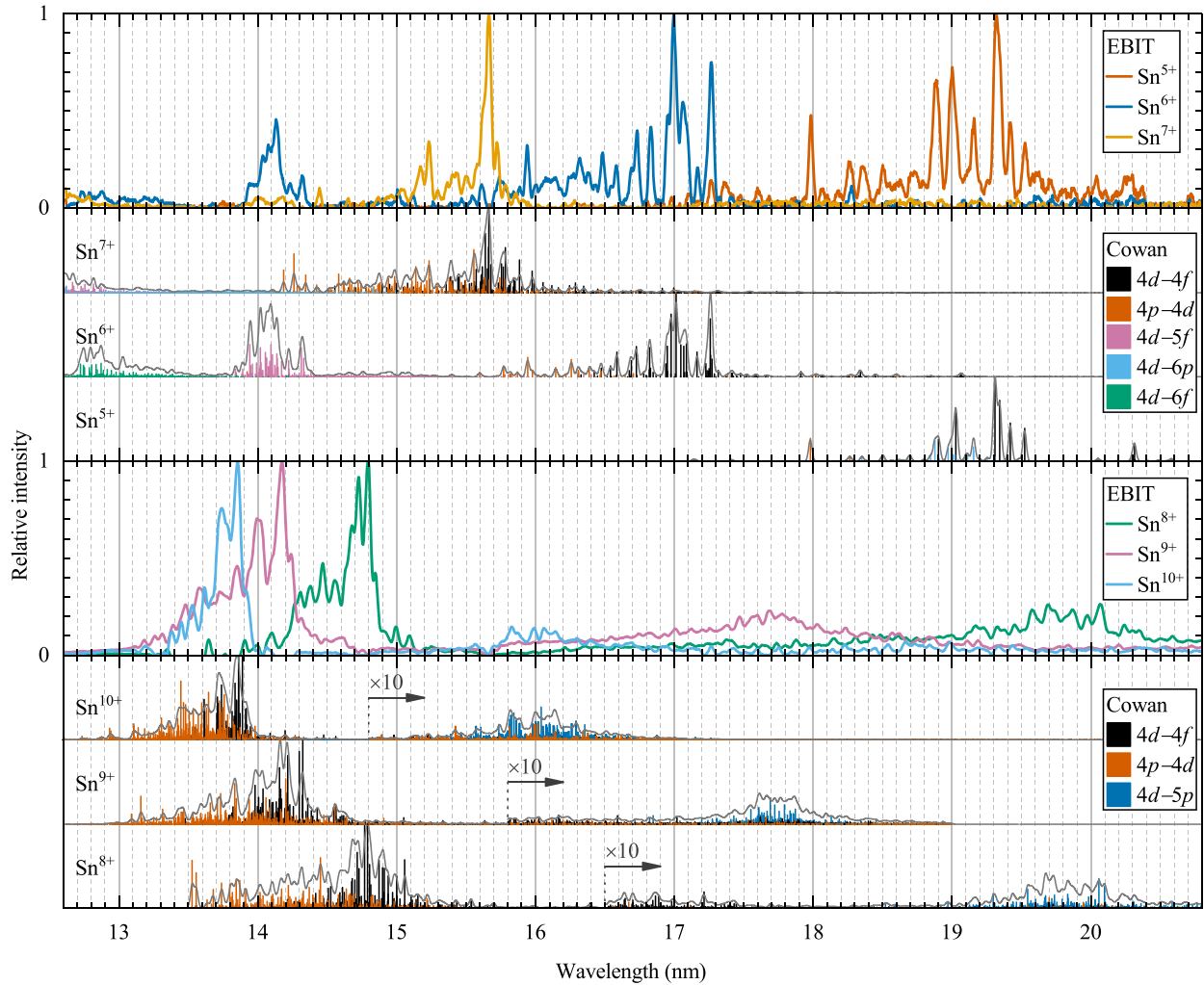
Figure 2. Normalized charge-state-resolved spectra from Sn^{5+}–Sn^{10+} ions obtained from the EBIT measurements using the matrix inversion method (see main text). The results for Sn^{5+}–Sn^{7+} originate from the 1.5 mA electron beam current measurements, and the Sn^{8+}–Sn^{10+} results derive from the 13 mA current measurements (see main text). Results from Cowan code calculations are presented with *gA* factors normalized to maximum *gA* value for the corresponding charge state (shown as sticks in the plot). The envelopes (shown in gray) represent a convolution of the *gA* factors with a Gaussian function accounting for the spectrometer resolution (0.03 nm FWHM). These envelopes are separately normalized to a maximum value of one at their respective maximum.

positions of relevant configurations is presented in figure 4 as well as in table 1. Next, the EBIT data is employed to qualitatively study the contribution of individual charge states to the emission from LPPs created from both droplet or planar solid tin targets (see figure 5).

3.1. EBIT spectra

In figure 1, a two-dimensional (wavelength–electron beam energy) spectral intensity colourmap of Sn ions constructed from EBIT measurements is presented (1.5 mA series). Emission features from Sn^{4+} to Sn^{10+} ions can be observed. The white line indicates the threshold at which the photon energy equals the electron beam energy, above which a particular transition can energetically be excited directly by single-electron impact.

The individual EBIT spectra contain a mixture of charge states, dependent on EBIT conditions such as electron beam energy and current. Following the procedure outlined in

reference [7], spectra of the individual charge states are obtained using a matrix inversion method. This method enables unraveling blended spectra by assuming that every spectrum contains a linear combination of contributions from individual charge states. The contributions from these charge states are weighted by their respective fluorescence curve (a curve defined as the emission intensity of the various spectral lines as function of the electron beam energy). Following the work of Scheers *et al* [7], to obtain fluorescence curves, we project vertical regions of interest from the data as shown in figure 1. Several lines per charge states are used to construct a generic fluorescence curve. Chosen lines are preferably isolated, mostly outside of dense spectral regions. The observed energy dependencies of the line strengths are typically very similar for all lines associated with a particular charge state. Individual fluorescence curves are normalized and subsequently averaged such that a generic fluorescence curve per charge is constructed. A matrix inversion technique is subsequently invoked. In it,
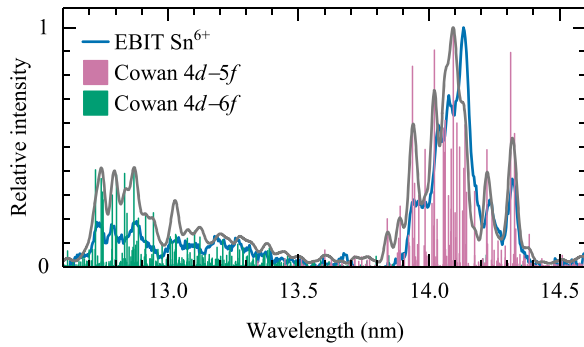
Figure 3. Identification of spectral features in Sn^{6+} obtained from the EBIT measurements using the matrix inversion method (see text). Vertical lines indicate calculated gA factors of $4d$–$(5f + 6f)$ transitions normalized to the strongest transition in this range. The gray envelope is a convolution of the presented gA values with a Gaussian function accounting for the spectrometer resolution of 0.03 nm (FWHM). The envelope is separately normalized for better visibility.

Figure 4. Wavelengths of spectral features of various transition arrays in Sn^{q+} ($q = 5$–10) as obtained from our Cowan code calculations. Symbol location represents the gA-weighted average wavelength of the transition array (first moment of the distribution according to UTA formalism [42, 43]), while the indicated width represents the standard deviation of the distribution (square root of the variance). Dashed vertical lines indicate a 2% bandwidth around 13.5 nm. Wavelengths and distribution widths shown in this figure are presented in table 1.

the colourmaps are represented by a matrix E. The matrix elements of contain spectral intensities directly obtained from measurements. Fluorescence curves span a fluorescence matrix F in $FS = E$, where S contains the individual, charge-state-resolved spectra. The solution of matrix S is given by $S = (F^T F)^{-1} F^T E$.

The charge-state-resolved spectra obtained from both the lower- and higher-current measurement series are nearly identical. An improved signal-to-noise ratio is obtained in the higher-current case. A consequence of using a different electron beam current might be variations in level population within the respective tin ions and therefore line intensities may change [37], but such an effect was not observed in our spectra. Because of the higher signal-to-noise ratio, the higher-current series is used in the following for the spectra of Sn^{8+}–Sn^{10+}. The lower-current series is used for Sn^{5+}–Sn^{7+} as these ions could not be observed in the higher-current series. Sn^{4+} is not included because its dominant line features largely fall outside the spectrometer range [6, 38].

In the following, the spectral fingerprints of the EBIT spectra from individual charge states are discussed. For convenience, the transitions of type of $4d^m$–$4d^{m-1}4f$, $4p^64d^m$–$4p^54d^{m+1}$, $4d^m$–$4d^{m-1}5f$, $4d^m$–$4d^{m-1}6p$, $4d^m$–$4d^{m-1}6f$ and $4d^m$–$4d^{m-1}5p$, where $m = 9$–4 in the case of Sn^{5+} to Sn^{10+}, will be written as $4d$–$4f$, $4p$–$4d$, $4d$–$5f$, $4d$–$6p$, $4d$–$6f$ and $4d$–$5p$, respectively.

The Hartree–Fock method with relativistic corrections incorporated in the RCN-RCN2-RCG chain of the Cowan code [23, 24] is used for the calculation of energy levels, transition wavelengths, and gA values (multiplicity g times the Einstein coefficient A). Spectral line intensities recorded from an EBIT may deviate from calculated gA values (see, e.g., reference [37]) as excited-state populations, which together with these gA values determine the line intensities, depend on the specifics of electron impact excitation. Inclusion of such effects in our calculations would require detailed collisional radiative modeling [39] which is beyond the scope of the current paper. In this work, we find that emission features can here be reliably identified using gA values.
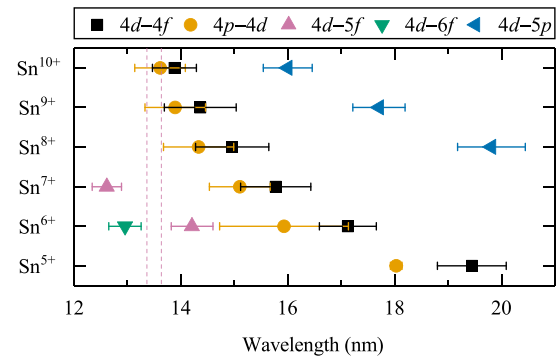
3.1.1. Spectrum of Sn^{5+}.
Strong emission line features of Sn^{5+} are observed between 18–20 nm in the EBIT spectrum (figure 2). These line features are related to transitions of type $4d$–$4f$ and $4d$–$6p$. They were identified in reference [15], where the Cowan code was used to analyze measurements performed using a spark source. A comparison between our spectrum with gA factors calculated by Cowan code using scaling parameters based on the line identifications from reference [15], convoluted with the spectrometer resolution (0.03 nm FWHM), is presented in figure 2. Calculations and experiment are in good agreement. Further, we observe a strong and isolated line at 17.98 nm wavelength. Cowan code calculations indicate that this feature can be identified as the $4p^6 \, 4d^9 \, {}^2D_{5/2}$–$4p^5 \, 4d^{10} \, {}^2P_{3/2}$ transition.

3.1.2. Spectrum of Sn^{6+}.
In the case of Sn^{6+}, prominent emission line features can be observed in figure 1 in three separate wavelength regions: 12.6–13.6 nm, 14–14.5 nm, and 16–17.5 nm. For the identification of the emission line features between 12.6–14.5 nm, we use the Cowan atomic structure code. The level energies of the $4d^75f$ and $4d^76f$ configurations of Sn^{6+} are optimized using configuration-interaction between the following configurations: $4p^6(4d^8 + 4d^75s + 4d^65s^2)$ in the even set and $4p^64d^7(5p + 6p + nf(n = 4$–$7)) + 4p^5(4d^9 + 4d^85s)$ in the odd set. The fitting of the levels of the $4p^64d^8$, $4p^64d^7(5p + 4f)$ and $4p^54d^9$ configurations was performed using known data [16, 40]. The electrostatic energy parameters of the unknown configurations $4d^76p$, $4d^77f$ and $4p^54d^85s$ were scaled by a rather standard factor 0.85 with respect to their *ab initio* Hartree–Fock with relativistic corrections (HFR) values. The interaction integrals were scaled by 0.8. The *ab initio* HFR values for the $4d^75f$ and $4d^76f$ configurations were improved using the same scaling factors and effective parameters as were obtained previously for $4d^74f$. The final fitted and adopted energy parameters as well as scaling factors for configurations $4d^7nf$ ($n = 4$–6) and $4p^54d^9$ responsible for most of the features in our EBIT spectrum,

J. Phys. B: At. Mol. Opt. Phys. **53** (2020) 195001

Z Bouza *et al*

including those in the 16–17.5 nm region, are presented in table 2.

The results of the Cowan code calculations for both $4d$–$5f$ and $4d$–$6f$ transitions are presented in figure 3, along with the spectrum of Sn^{6+} obtained from the matrix inversion technique. The heights of the vertical lines represent the calculated gA values for individual lines within the transition arrays $4d$–$(5f + 6f)$. They are normalized to the strongest transition in the here-presented wavelength range. The gray envelope is a convolution of these gA factors with a Gaussian function representing the spectrometer resolution (0.03 nm FWHM). This envelope is separately normalized to a value of one for better visibility. The EBIT spectrum of Sn^{6+} presents a smaller relative emission amplitude, by a factor of approximately two, in the 12.6–13.2 nm range as would be expected from a direct comparison of the calculated gA values of the $4d$–$5f$ to the $4d$–$6f$ transitions. This relatively small amplitude may in part be explained by the fact that the electron beam energy is barely sufficient to excite to the levels giving rise to the $4d$–$6f$ transitions. Collisional radiative modeling, left for future work, would enable assessing the dependence of the observed line strengths on electron beam energy and its density. In general, our calculations, including those for the $4d$–$4f$ and $4p$–$4d$ transitions, are in good agreement with the spectra (see figure 2).

3.1.3. Spectrum of Sn^{7+}. Emission line features of Sn^{7+} lie between 15–16 nm, as seen from figure 2. These line features correspond to the $4d$–$4f$, $4p$–$4d$ transitions identified by Churilov and Ryabtsev [12] employing a vacuum spark setup. Figure 2 also shows transition probabilities for the Sn^{7+} ion spectrum calculated with the Cowan code using scaling parameters from reference [12]. A convolution of these transitions with Gaussian function accounting for the spectrometer resolution is in agreement with the experimental spectrum. The $4d$–$6p$ transitions are not visible in our EBIT spectra. However, we note that our calculations of the $4d$–$6p$ transitions are in excellent agreement with unidentified spectral features around 14 nm observed in CXS, whereby spectra resulting from collisions of Sn^{8+} with He and Xe were observed [6]. The small feature at the edge of our detection region (near 12.8 nm) may be tentatively associated with the $4d$–$5f$ transition array as was previously noted in reference [13].

3.1.4. Spectrum of Sn^{8+}. Strong emission features of Sn^{8+} are found between 14 and 15 nm, as shown in figure 2. Identified lines stem from $4p$–$4d$ and $4d$–$4f$ transitions [11]. Although more recent studies [31] have found that the level energies of the ground manifold from [11] in Sn^{8+}–Sn^{10+} may not be fully correct, the accuracy of the line determination in the EUV is sufficient for the current investigations. Configurations used in those [11] and the current Cowan calculations for the charge states Sn^{8+}–Sn^{10+} are of type $4d^{m-1}(5p + 6p) + 4d^{m-1}(4f + 5f + 6f) + 4p^5(4d^{m+1} + 4d^m5s)$. Scaling factors were estimated by extrapolation from Sn^{6+}, Sn^{7+}, and isoelectronic Ag ion spectra [41]. The results, shown in figure 2, are in agreement with our measurements. Emission features located near 20 nm belong to the $4d$–$5p$ transition array in Sn^{8+}–Sn^{10+} ions, as previously identified by Ohashi and

Table 1. Average wavelength of various transition arrays in Sn^{q+} ($q = 5$–10), see also figure 4. Results obtained from the Cowan code are presented as gA-weighted average wavelength of the transition array (first moment of the distribution according to UTA formalism [42, 43]), and the width represents the standard deviation of the distribution (square root of the variance). CXS results (center of distribution of emission lines) are obtained from collisions of $Sn^{(q+1)+}$ with Xe, reproduced from reference [6]. We note that the table entries from reference [6] may refer to the average position of the $4d$–$4f$ and $4p$–$4d$ transitions arrays combined.

		Average wavelength (nm)		
Ion	Transition	CXS [6]	COWAN	Width (nm)
Sn^{5+}	$4d$–$4f$	19.0	19.4	0.6
	$4p$–$4d$	—	18.0	0.1
Sn^{6+}	$4d$–$4f$	16.0	17.1	0.5
	$4p$–$4d$	—	15.9	1.2
	$4d$–$5f$	—	14.2	0.4
	$4d$–$6f$	—	13.0	0.3
Sn^{7+}	$4d$–$4f$	15.6	15.8	0.7
	$4p$–$4d$	—	15.1	0.6
	$4d$–$5f$	12.5	12.6	0.3
Sn^{8+}	$4d$–$4f$	14.2	15.0	0.7
	$4p$–$4d$	—	14.3	0.7
	$4d$–$5p$	19.5	19.8	0.6
Sn^{9+}	$4d$–$4f$	14.0	14.4	0.7
	$4p$–$4d$	—	13.9	0.6
	$4d$–$5p$	17.7	17.7	0.5
Sn^{10+}	$4d$–$4f$	13.8	13.9	0.4
	$4p$–$4d$	—	13.6	0.5
	$4d$–$5p$	16.0	16.0	0.5

coworkers [6] in their CXS work. No individual line assignments were made in that work. There are thousands of lines contributing to these features, thus making line identifications of specific transitions inaccessible, which is also true in the current work. However, the origin of the emission features can be well understood from Cowan code calculations.

3.1.5. Spectrum of Sn^{9+}. The $4p$–$4d$ and $4p$–$4f$ transitions of Sn^{9+} are located around 14 nm, as shown in figure 2, and line identifications are described in reference [11]. A comparison of the spectrum, as obtained by the matrix inversion technique, with the listed transitions of reference [11] show that the strongest peak at 14.17 nm cannot be satisfactorily explained. However, using instead Cowan calculations based on an extrapolation of scaling factors, similar to the case of Sn^{8+} (see above), enables obtaining a reasonable match with the experimental spectrum (see figure 2) including the $4d$–$5p$ transitions located between 16 and 19 nm.

3.1.6. Spectrum of Sn^{10+}. The $4p$–$4d$ and $4d$–$4f$ transitions in Sn^{10+} are found between 13 and 14 nm (figure 2) according to line identifications performed on this transition array in reference [11]. Transitions of the type $4d$–$5p$ are observed between 15 and 17 nm. The Cowan calculations (for details, see above) for the aforementioned transition arrays are in excellent agreement with the experimental data, as shown in figure 2.
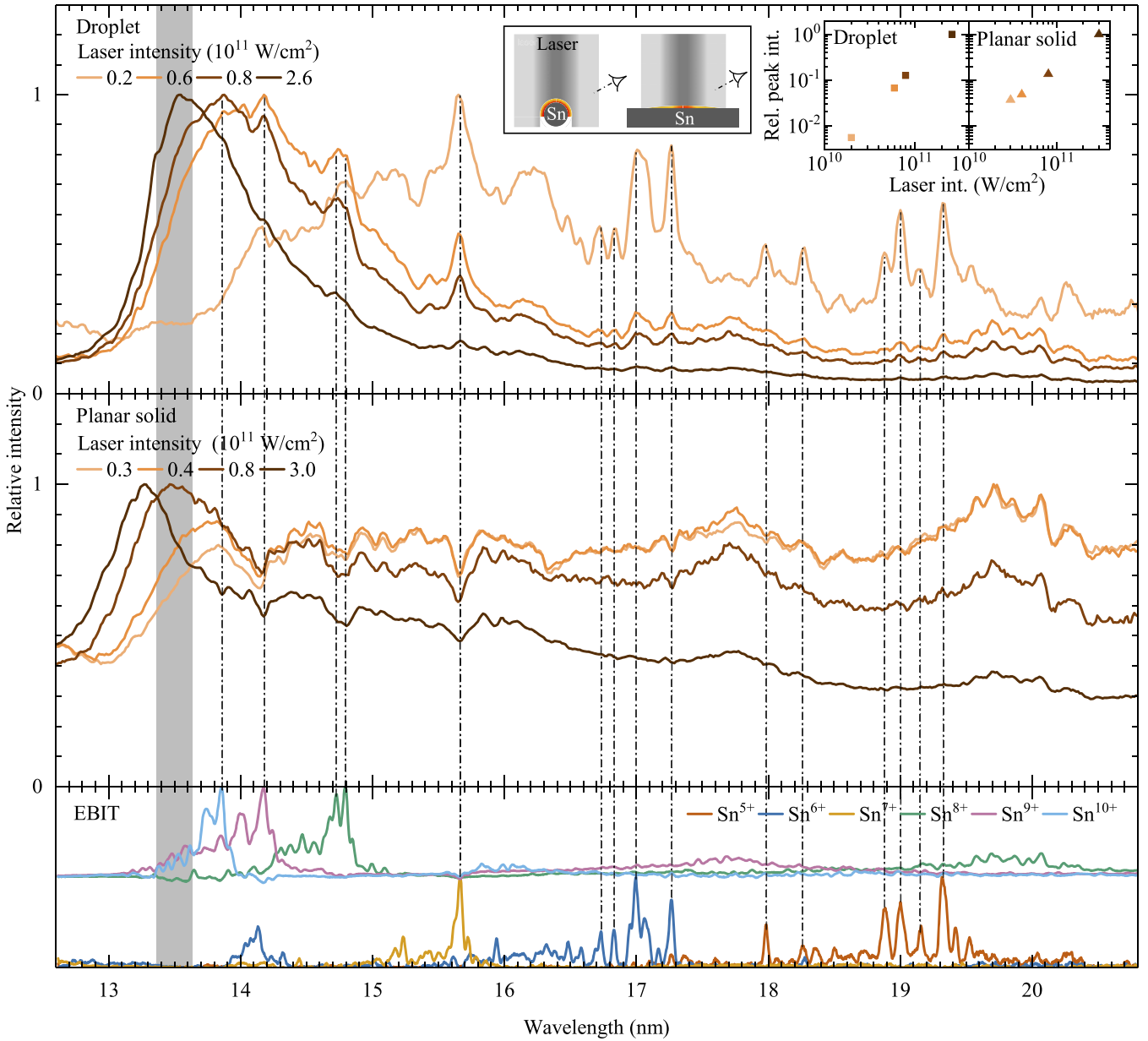
Figure 5. Top: normalized experimental LPP emission spectra in the EUV range for various Nd:YAG laser intensities, using a liquid droplet-based tin target with a droplet diameter of 18 μm and an FWHM laser beam spot of 80 μm. Middle: normalized experimental LPP emission spectra in the EUV region for various Nd:YAG laser intensities, using a planar solid tin target with a laser beam spot of 130 μm FWHM. Bottom: normalized charge-state-resolved spectra of $Sn^{5+}-Sn^{10+}$ obtained from the EBIT measurements using the matrix inversion method (see text); the spectra of the three highest charge states are vertically offset for better visibility. The gray-shaded area shows the 2% bandwidth around 13.5 nm relevant for nanolithographic applications. The vertical dashed-dotted lines trace particular features from the EBIT in the LPP spectra. A schematic layout of both LPP experiments is presented as an inset in the top panel. The additional inset graph shows relative peak intensities as a function of laser intensity for both target cases.

3.1.7. Summary of EBIT spectra. Figure 4 summarizes our findings of the emission characteristics of the $4d-4f$, $4p-4d$, $4d-5f$, $4d-6f$, and $4d-5p$ transitions of the charge states $Sn^{5+}-Sn^{10+}$. We note that the positions found for the $4d-4f$ and $4p-4d$, smoothly scaling with charge state, are in accordance with literature values. These configurations become more and more intertwined with increasing charge state. We note that the $4d-5p$ transitions in $Sn^{8+}-Sn^{10+}$ may be easily confused with $4d-4f$ or $4p-4d$ transitions of the lower charge states when diagnosing a tin plasma.

3.2. Diagnosing LPP spectra

Figure 5 presents EUV emission spectra for various laser intensities from LPPs using two target geometries: droplet and planar-solid. Plasma is produced from a Sn droplet target (top panel) and from a planar solid target (middle panel). Charge-state-resolved EBIT spectra of $Sn^{5+}-Sn^{10+}$ ions are shown also (bottom panel).

In the top panel of figure 5, emission spectra from illumination of a Sn droplet target using laser intensities of

Table 2. Cowan code (HFR) corrections and least-square-fitted parameter values of the $4d^7nf$ ($n = 4$–6), and $4p^54d^9$ configurations in Sn^{6+}. All parameters are given in units of cm^{-1}. One-standard-deviation uncertainties are given in brackets. Fixed parameters are indicated with a superscripted 'f'. Parameters superscripted with r1, r2, and r3 are also fixed in the fitting procedure.

	$4d^74f$			$4d^75f$		$4d^76f$	
Parameter	HFR	FIT	FIT/HFR	HFR	Adopted	HFR	Adopted
$E_{average}$ $(4d^7nf)$	535 000	533 917 (271)		694 284	693 283	779 714	779 714
$F^2(4d, 4d)$	102 377	85 801 (200)	0.838	103 411	86 649	103 642	86 843
$F^4(4d, 4d)$	68 285	59 966 (468)	0.878	69 065	60 650	69 238	60 802
$\alpha(4d)$		50^f		50			50
$\beta(4d)$		-540^f		-540			-540
$T^1(4d)$		-2^f		-2			-2
$\zeta(4d)$	3681	3799^f	1.032	3740	3861	3757	3877
$\zeta(nf)$	110	110^f	1	52	52	28	28
$F^2(4d, nf)$	65 286	54 159 (1254)	0.829^{r1}	22 023	18 257	10 343	8574
$F^4(4d, nf)$	40 129	33 290 (771)	0.829^{r1}	12 342	10 232	5631	4669
$G^1(4d, nf)$	75 280	60 314 (331)	0.801^{r2}	20 272	16 238	8371	6705
$G^3(4d, nf)$	45 662	36 584 (201)	0.801^{r2}	13 362	10 703	5781	4630
$G^5(4d, nf)$	31 866	25 530 (140)	0.801^{r2}	9627	7711	4241	3397
	$4p^54d^9$						
Parameter	HFR	FIT	FIT/HFR				
$E_{average}$ $(4p^54d^9)$	616 908	597 881 (506)	0.969				
$\zeta(4p)$	40 711	44 357 (539)	1.09				
$\zeta(4d)$	3599	3714^f	1.032				
$F^2(4d, 4d)$	108 221	102 669 (3811)	0.949				
$G^1(4p, 4d)$	137 494	107 607 (1666)	0.783^{r3}				
$G^3(4p, 4d)$	85 454	66 898 (1035)	0.783^{r3}				

0.2, 0.6, 0.8, and 2.6×10^{11} W cm^{-2} are presented. The laser intensity was calculated as described in reference [34]. The dependence of the main feature near 13.5 nm wavelength on laser intensity has been discussed in detail elsewhere (see, e.g., reference [34, 44]) and the current discussion focuses on the wavelengths above 13.5 nm. For the lowest laser intensity, line features associated with the $4d$–$4f$ transition arrays in Sn^{5+}–Sn^{7+} particularly stand out. Their visibility strongly decreases with increasing laser intensity. Instead, line features associated with $4d$–$5p$ transitions of the more highly charged Sn^{8+} and Sn^{9+} ions become more prominent in this wavelength range with increasing laser intensity. The reduction of observed intensities of lines associated with the lower charge states is most pronounced for Sn^{5+} and Sn^{6+}; lines of Sn^{7+} also reduce in relative amplitude but remain visible for all laser intensities shown. The expected evolution of the apparent charge state distribution with laser intensity is thus observed: higher laser intensity produce a hotter plasma with a higher average charge state. A more quantitative study would yield important insights regarding the population of charge states relevant for in-band emission at 13.5 nm wavelength, analogous and complementary to the work of Torretti *et al* [22] for the shorter-wavelength emission features.

In the middle panel of figure 5, emission spectra are shown from a planar solid tin target for laser intensities of 0.3, 0.4, 0.8, and 3.0×10^{11} W cm^{-2}. This series of intensities is similar to those used in the droplet target case. The spectral differences between planar solid and droplet targets for wavelengths larger than 14 nm are striking. Generally, much more

emission occurs at these longer wavelengths than in to the droplet target case. No emission line features of the low charge states Sn^{5+}–Sn^{7+} stand out. Instead, for all laser intensities, the $4d$–$5p$ transitions of the more highly charged Sn^{8+}–Sn^{10+} ions dominate this part of the spectrum. These emission features slowly decrease in relative amplitude as the laser intensity increases. Noteworthy are dips in the spectra observed at wavelengths where emission peaks appear for the droplet target. More specifically, the strong dip around 15.6 nm seems to coincide with the expected location of the $4d$–$4f$ + $4p$–$4d$ transition array of Sn^{7+}. Similarly, two other particularly visible dips, located around 14.8 nm and 14.2 nm, line up with $4d$–$4f$ + $4p$–$4d$ transitions of Sn^{8+} and Sn^{9+}, respectively. The latter dip position also overlaps with the $4d$–$5f$ transition in Sn^{6+}. These dips can thus be explained by absorption by the plasma constituents.

Briefly, the spectral differences between the two target cases can be traced to geometrical arguments. The particular initial phase (liquid vs planar solid tin) has little bearing on the ensuing plasma given the energies involved. The geometry of the target affects the plasma emission in two aspects. First, size: the small, 18 μm diameter droplet interacts mainly with the most intense part of the 80 μm laser pulse spot. In contrast, the large solid target interacts with the full beam spot. Second, dimensionality: the plasma expands and rarefies. The dimensionality of the rarefaction can be related to that of the target: a one-dimensional, linear expansion for the planar target and a quasi-three-dimensional expansion for the small droplet [45]. The rarefaction is much more rapid in the droplet case leading

J. Phys. B: At. Mol. Opt. Phys. **53** (2020) 195001

Z Bouza *et al*

to less (self-)absorption of light [34]. Thus, the absorption features of the solid target spectra may be attributed to absorption in a rather dense but colder part of the plasma, which contains the relevant charge states that exhibit significant opacity [18], surrounding the main, hot and dense emission zone [46, 47]. For near-infrared drive lasers such as those operating at 1 μm wavelength, a spherical target appears to be better suited for obtaining a large fraction of the emitted EUV radiation in-band.

4. Conclusion

Emission spectra from multiply-charged Sn^{5+}–Sn^{10+} ions are recorded from an EBIT and from LPP in the EUV range. In particular, features in the wavelength range between 12.6 and 20.8 nm are studied. A matrix inversion method is employed to produce charge-state-resolved spectra from the EBIT measurements. The Cowan code is used to identify the emission line features. Particular attention is given to the newly identified $4d$–$5f$ and $4d$–$6f$ transitions in Sn^{6+}. We have also identified a previously unreported $4p$–$4d$ transition in Sn^{5+}. The obtained spectroscopic information is employed to diagnose the Sn LPP produced from a liquid droplet and a planar solid Sn target. Emission features are identified and assigned to specific charge states using the EBIT data. For the planar solid Sn target, the $4d$–$5p$ transitions of Sn^{8+}–Sn^{10+} ions dominate the long-wavelength part of the EUV spectrum. Transitions of type $4d$–$4f$ + $4p$–$4d$ appear as self-absorption dips in the spectra. For the droplet target relevant for nanolithography, a more clear evolution of the charge state distribution with laser intensity is observed: higher laser intensities produce a hotter plasma with a higher average charge state. Transitions of type $4d$–$4f$ + $4p$–$4d$ in Sn^{5+}–Sn^{7+} smoothly give way to $4d$–$5p$ type transitions in Sn^{8+}–Sn^{10+}. This study demonstrates the inherent potential of out-of-band emission to individually monitor several Sn charge states that strongly contribute to the unresolved transition array at 13.5 nm.

ORCID iDs

Z Bouza ⓘ https://orcid.org/0000-0001-8583-9929
J Scheers ⓘ https://orcid.org/0000-0002-3627-8755
R Schupp ⓘ https://orcid.org/0000-0002-6363-2350
C Shah ⓘ https://orcid.org/0000-0002-6484-3803
J Sheil ⓘ https://orcid.org/0000-0003-3393-9658
M Bayraktar ⓘ https://orcid.org/0000-0002-8339-2091
J R Crespo López-Urrutia ⓘ https://orcid.org/0000-0002-2937-8037
W Ubachs ⓘ https://orcid.org/0000-0001-7840-3756
R Hoekstra ⓘ https://orcid.org/0000-0001-8632-3334
O O Versolato ⓘ https://orcid.org/0000-0003-3852-5227

References

[1] Benschop J, Banine V, Lok S and Loopstra E 2008 *J. Vac. Sci. Technol.* B **26** 2204
[2] Banine V Y, Koshelev K N and Swinkels G H P M 2011 *J. Phys. D: Appl. Phys.* **44** 253001
[3] O'Sullivan G *et al* 2015 *J. Phys. B: At. Mol. Opt. Phys.* **48** 144025
[4] Versolato O O 2019 *Plasma Sources Sci. Technol.* **28** 083001
[5] Tolstikhina I Y, Churilov S S, Ryabtsev A N and Koshelev K N 2006 *EUV Sources for Lithography* ed V Bakshi (Bellingham, WA: SPIE Optical Engineering Press) ch 4 pp 113–48
[6] Ohashi H, Suda S, Tanuma H, Fujioka S, Nishimura H, Sasaki A and Nishihara K 2010 *J. Phys. B: At. Mol. Opt. Phys.* **43** 065204
[7] Scheers J *et al* 2020 *Phys. Rev.* A **101** 062511
[8] Bajt S, Alameda J B, Barbee T W Jr, Clift W M, Folta J A, Kaufmann B B and Spiller E A 2002 *Opt. Eng., Bellingham* **41** 1797
[9] Huang Q, Medvedev V, van de Kruijs R, Yakshin A, Louis E and Bijkerk F 2017 *Appl. Phys. Rev.* **4** 011104
[10] Churilov S S and Ryabtsev A N 2006 *Opt. Spectrosc.* **101** 169
[11] Churilov S S and Ryabtsev A N 2006 *Phys. Scr.* **73** 614
[12] Churilov S S and Ryabtsev A N 2006 *Opt. Spectrosc.* **100** 660
[13] Svendsen W and O'Sullivan G 1994 *Phys. Rev.* A **50** 3710
[14] Ryabtsev A N, Kononov É Y and Churilov S S 2008 *Opt. Spectrosc.* **105** 844
[15] Churilov S S, Kildiyarova R R, Ryabtsev A N, Kramida A and Joshi Y N 1994 *Phys. Scr.* **50** 463
[16] Azarov V I, Joshi Y N, Churilov S S and Ryabtsev A N 1994 *Phys. Scr.* **50** 642
[17] D'Arcy R *et al* 2009 *Phys. Rev.* A **79** 042509
[18] Torretti F *et al* 2020 *Nat. Commun.* **11** 1
[19] Liu K, Li Y, Zhang F and Fan M 2007 *Jpn. J. Appl. Phys.* **46** 6568
[20] Yang G and Li Y 2012 *Extreme Ultraviolet (EUV) Lithography III* vol 8322 (International Society for Optics and Photonics) p 83222V
[21] Torretti F, Schupp R, Kurilovich D, Bayerle A, Scheers J, Ubachs W, Hoekstra R and Versolato O O 2018 *J. Phys. B: At. Mol. Opt. Phys.* **51** 045005
[22] Torretti F, Liu F, Bayraktar M, Scheers J, Bouza Z, Ubachs W, Hoekstra R and Versolato O 2019 *J. Phys. D: Appl. Phys.* **53** 055204

J. Phys. B: At. Mol. Opt. Phys. **53** (2020) 195001

Z Bouza *et al*

[23] Cowan R D 1981 *The Theory of Atomic Structure and Spectra* (Berkeley, CA: University of California Press)

[24] Kramida A 2019 *Atoms* **7** 64

[25] Epp S W *et al* 2010 *J. Phys. B: At. Mol. Opt. Phys.* **43** 194008

[26] Harada T and Kita T 1980 *Appl. Opt.* **19** 3987

[27] Baumann T M 2012 Spektroskopische Untersuchungen resonanter Rekombinationsprozesse an hochgeladenem Silizium in einer Elektronenstrahl-Ionenfalle *PhD Thesis* Ruprecht-Karls-Universität, Heidelberg

[28] Liang G Y *et al* 2009 *Astrophys. J.* **702** 838

[29] Kramida A, Ralchenko Y and Reader J(NIST ASD Team) 2015 *NIST Atomic Spectra Database* (*ver. 5.3*) (Gaithersburg, MD: National Institute of Standards and Technology) http://physics.nist.gov/asd

[30] Windberger A *et al* 2016 *Phys. Rev.* A **94** 012506

[31] Torretti F *et al* 2017 *Phys. Rev.* A **95** 042503

[32] Goh S J, Bastiaens H J M, Vratzov B, Huang Q, Bijkerk F and Boller K J 2015 *Opt. Express* **23** 4421

[33] Bayraktar M, Bastiaens H M J, Bruineman C, Vratzov B and Bijkerk F 2016 *NEVAC Blad* **54** 14

[34] Schupp R *et al* 2019 *Phys. Rev. Appl.* **12** 014010

[35] Kurilovich D, Klein A L, Torretti F, Lassise A, Hoekstra R, Ubachs W, Gelderblom H and Versolato O O 2016 *Phys. Rev. Appl.* **6** 014018

[36] Bayerle A *et al* 2018 *Plasma Sources Sci. Technol.* **27** 045001

[37] Bekker H *et al* 2015 *J. Phys. B: At. Mol. Opt. Phys.* **48** 144018

[38] Churilov S S, Joshi Y N and Ryabtsev A N 1994 *J. Phys. B: At. Mol. Opt. Phys.* **27** 5485

[39] Ralchenko Y V and Maron Y 2001 *J. Quant. Spectrosc. Radiat. Transfer* **71** 609

[40] van het Hof G J and Joshi Y N 1993 *Phys. Scr.* **48** 714

[41] Ryabtsev A, Kildiyarova R and Kononov E 2017 *Atoms* **5** 47

[42] Bauche J, Bauche-Arnoult C and Klapisch M 1988 *Adv. At. Mol. Phys.* **23** 131

[43] Bauche J, Bauche-Arnoult C and Peyrusse O 2015 *Atomic Properties in Hot Plasmas* (Berlin: Springer)

[44] Schupp R *et al* 2019 *Appl. Phys. Lett.* **115** 124101

[45] Basko M M, Novikov V G and Grushin A S 2015 *Phys. Plasmas* **22** 053111

[46] Lysaght M, Kilbane D, Murphy N, Cummings A, Dunne P and O'Sullivan G 2005 *Phys. Rev.* A **72** 014502

[47] Fujioka S *et al* 2005 *Phys. Rev. Lett.* **95** 235004